Lab on a Chip

PAPER

View Article Online
View Journal

Cite this: DOI: 10.1039/d5lc00898k

Real-time impedance-based cell migration measurements with integrated electrodes on porous membranes for next generation microphysiological systems

Karina Torres-Castro , †‡[ab] Aditya Rane ‡[ab] and Darwin R. Reyes *[a]

We present a novel microfluidic device capable of electrically interrogating both surfaces of a porous membrane quantitatively and in real time using electrical impedance spectroscopy to monitor cell migration. This device holds patterned gold electrodes on both sides of the membrane, which enable independent impedance measurements on each side of the membrane. We introduce the term cross-over cell migration (CoCM) to describe this dual-sided approach, which allows precise monitoring of cells at their seeding location and as they move through a porous membrane. To ensure reliable tracking, we developed a normalization method, the CoCM index, that allows us to compare both membrane surfaces directly in real-time. Human renal carcinoma cells (786-O) were passively seeded in the device's top microfluidic chamber, and we collected impedance data from both sides of the membrane surfaces simultaneously over a three-day period. These measurements successfully captured the onset and progression of cell migration across the membrane interface. We tracked the cells with fluorescence imaging in parallel to validate our impedance data. As cells appeared in focus on the bottom-side electrode surface, their numbers kept increasing over the course of our experiment. The CoCM index decreased by about 20% in the top chamber and increased by approximately 15% in the bottom chamber. Symmetrical CoCM index trends appeared after 40 h, consistent with the fluorescent images captured. Finally, we performed live-cell fluorescence assays to confirm post-experiment cell viability and to quantify migrated cells, further validating our CoCM platform measurements. This platform is a valuable tool not only for real-time and quantitative cell migration studies of cancer and other cells in bulk but also for future studies of single-cell migration processes.

Received 19th September 2025,
Accepted 14th February 2026

DOI: 10.1039/d5lc00898k

rsc.li/loc

1 Introduction

Cell migration plays a crucial role in many physiological, developmental, and disease-related processes. But in addition to helping maintain healthy tissue, cell migration also affects cellular processes under pathological states such as inflammatory diseases,[1] immune responses,[2] and cancer.[3] For instance, defective cell migration can disrupt neuronal development, inhibit chronic wound healing, and cause immune deficiencies. Furthermore, uncontrolled cell migration can lead to invasive metastatic cancer, autoimmune diseases, and fibrosis.[4]

Cells respond and migrate distinctly based on the environmental cues they are presented with, including mechanical substrate compliance (durotaxis) and stiffness,[5] geometric features such as porosity and surface roughness,[6] electric cues (electrotaxis),[7] chemical cues on surfaces (haptotaxis),[8] and chemical diffusion (chemotaxis).[9] However, understanding how cells migrate through different body cavities and porous tissues provides valuable insights into *in vivo* migration mechanisms, as well as how cells communicate and interact with each other.[10,11] For example, different tissue cells can be cultured on the top and bottom of a centrally located, extracellular matrix-coated porous membrane, with air introduced in one of the channels for lung-on-a-chip studies or with the perfusion of different fluids to test the effects of various drugs or fluid characteristics on cell–cell interactions in brain-on-a-chip and heart-on-a-chip models.[12]

In vitro studies have shown that subpopulations of cells can create short-range dynamic gradients[13] that stimulate

[a] *National Institute of Standards and Technology (NIST), 100 Bureau Drive, Gaithersburg, MD 20899, USA. E-mail: darwin.reyes@nist.gov*
[b] *Theiss Research, 7411 Eads Ave, La Jolla, CA 92037-5037, USA*
† Current address: Department of Mechanical Engineering, Stony Brook University, Stony Brook, NY 11794, USA.
‡ These authors contributed equally to this work.

directional migration in other cells, similar to a leader-follower dynamic.[14] Therefore, monitoring cell migration in real-time through thin membranes can generate critical knowledge regarding these dynamic processes. Furthermore, sensing approaches for real-time monitoring of cell migration dynamics can provide new insights if integrated into 3D microphysiological systems (MPS) and are label-free. Label-free sensing techniques are preferable since they do not chemically modify cells, thus eliminating the possibility of cells developing additional interactions when exposed to molecules foreign to the human body. Among the label-free analytical methods available for monitoring cell behavior, electrochemical impedance spectroscopy (EIS) provides great compatibility with MPS,[15] continuous readout, and amenable coupling with complementary techniques such as optical microscopy.[16–18]

Several research groups have integrated impedance sensing capabilities into cell culture wells,[19,20] transwells (Boyden chambers),[21] and microfluidic channels.[22] Among commercially available solutions, a real-time cell analyzer using transwells with porous membranes containing patterned microelectrodes on one side of the membrane has been reported.[23,24] In this commercial system, cells are seeded on the top surface of the membrane within a gel layer (*e.g.*, Matrigel), and the platform detects them only after they have migrated to the opposite side. While this platform uses a normalization method to quantify impedance changes over time, in which the overall cell index increases as cells cross the membrane, this approach provides impedance information from only one side.[25] Consequently, it cannot capture the complete movement across the membrane. Moreover, seeding cells in a gel increases the migration distance before they reach the membrane interface, and the quasi-static well configuration is limited to batch-mode operation, preventing integration into microfluidic platforms, which offer higher impedance sensitivity and precise flow control necessary for various MPS applications.

Other approaches that integrate impedance measurements into microfluidic devices[26,27] have become more sophisticated in their attempts to sense the movement of cell clusters or to increase sensitivity for single-cell measurements.[28] However, these approaches share the common limitation of placing electrodes on only solid surfaces such as the substrate and/or the ceiling of the channels (*e.g.*, glass, plastic, silicon) and, as a result, can only measure cells when they depart or arrive at the electrodes.

Another approach for transepithelial/transendothelial electrical resistance (TEER)[29,30] measurements consists of a microfluidic device with a channel divided by a porous membrane and electrodes fabricated at the floor of the bottom channel and the ceiling of the top channel. In this system, a cell layer is measured from top to bottom across the membrane. This design enables real-time measurements of the integrity and permeability of cell barriers across the membrane, but cannot measure the impedance directly at the interface where the cells are.[31] Although innovative, this approach limits single-cell sensitivity, as the sensing mechanism relies on bulk impedance measurements across both microfluidic channels rather than directly measuring the location of the cells.

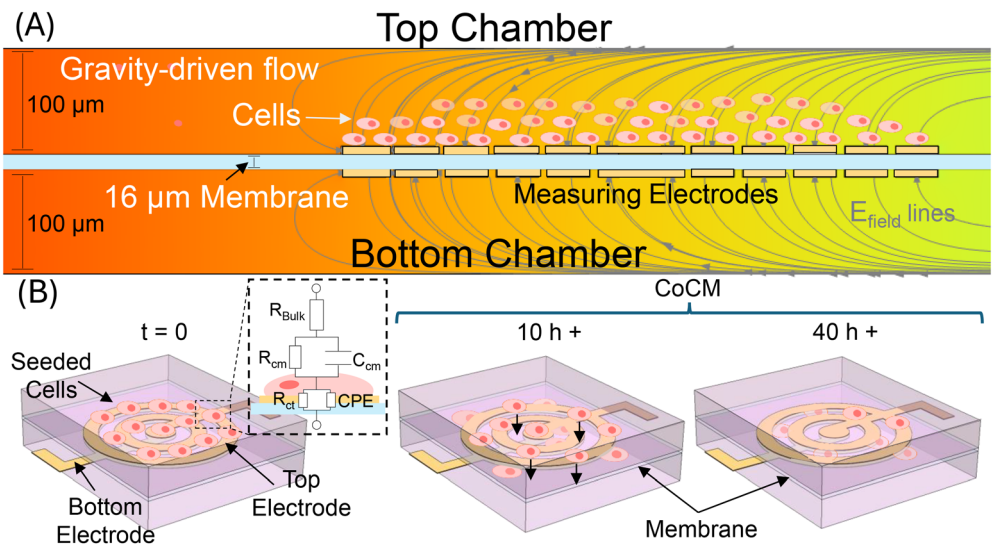

Fig. 1 Concept of cross-over cell migration (CoCM) impedance measurements. (A) Lateral view of the microfluidic chamber cell seeding process *via* passive flow. The chamber is divided by a porous membrane (light blue), with measurement electrodes on both sides of the membrane. The pressure gradient and electric field lines are also illustrated. (B) At t = 0 h, the cells are settled on the top electrodes located in the upper microfluidic chamber. The inset shows a previously reported equivalent circuit model for cell migration impedance measurements, where R_{Bulk} represents the bulk resistance of the cell medium; R_{cm} and C_{cm} denote the cell membrane resistance and capacitance, respectively; and R_{ct} and a constant phase element (CPE) capacitance represent the charge transfer resistance and the electric double layer at the electrode surface.[32] Cells re-arrange, spread, and begin migrating towards the bottom chamber through the membrane after ≈10 h, where they are probed by the bottom measurement electrodes. After ≈40 h, a larger cluster of cells migrates into the bottom channel.

To address these limitations, we developed an approach that can independently measure cell behavior at the surface and on both sides of the membrane. This method, combined with a normalization technique allow us to monitor in real-time and continuously cell migration processes on both sides of the membrane. The system consists of interdigitated electrodes on both sides of a track-etched polyethylene terephthalate (PET) membrane. This allows us to monitor cell migration in a microfluidic chamber by measuring the cross-over cell migration or CoCM impedance of cells traversing a porous membrane. Our device concept is shown in Fig. 1(A and B).

We seeded 786-O adenocarcinoma kidney cells passively (pump-free) onto the PET membrane in a microfluidic chamber and developed a CoCM index normalization method that allows us to track both sides of the porous membrane (top and bottom chambers) and standardize the measurements for the two potentiostats we used to measure both surfaces. Therefore, our CoCM impedance index enables us to track cells, simultaneously and with two separate instruments, as they cross the porous membrane interface.

To the best of our knowledge, this is the first microfluidic platform capable of tracking cell migration across a porous membrane by measuring impedance fluctuations on both sides of the membrane surface, effectively monitoring CoCM impedance in real-time. This platform can also be operated with microfluidic pumps for various MPS applications, such as heart-on-a-chip and to track changes in cell morphology due to interstitial shear stress or different flow conditions at porous interfaces that emulate human tissue structures. Both applications are the subject of current research in our lab.

2 Materials and methods

Fabrication and assembly of CoCM impedance device

We developed a novel CoCM device consisting of two vertically aligned chambers separated by a porous PET membrane, with addressable electrodes integrated on both sides to allow simultaneous and independent impedance measurements on each surface. Commercially available track-etched PET membranes (2000M23, it4ip S.A.) with an 8 μm pore diameter (6×10^4 cm^{-2}) and 16 μm thickness were cleaned in isopropyl alcohol (IPA) and deionized water (DI H_2O). To pattern electrodes on the porous membranes, each membrane was placed on a Si wafer with a spun-on high modulus reprographic silicone (hPDMS, Gelest§) coating (Fig. 2A(i and ii)). The hPDMS on the Si wafer serves as a substrate to adhere the thin, track-etched membrane, allowing for downstream photolithography-based techniques at a wafer scale. Gold electrodes 50 μm wide, and separated by gaps of 5 μm (see Fig. S1 for SEM image of electrodes on membrane), were then patterned on both sides of the membrane using a modified version of the method previously developed in our lab.[33,34] Briefly, a photoresist bilayer of lift-off resist (LOR 3A, Kayaku Advanced Materials) and photoresist S1813 (Kayaku Advanced Materials) was spin-coated on the membranes (Fig. 2A(iii)). After soft baking the resists, the membranes were exposed using a maskless aligner to pattern the electrode design. Membranes were developed using MF319 developer (Kayaku Advanced Materials), followed by deposition of a 5 nm Ti layer and a 50 nm Au layer using a Denton E-beam evaporator. The metal layers were then lifted off using PG Remover (Kayaku Advanced Materials) and Remover 1165 (Kayaku Advanced Materials), and lift-off to pattern interdigitated electrodes and a counter electrode on one side of the membrane (Fig. 2A(iv)). The patterned membrane was then flipped over to repeat the process and pattern electrodes on the other side of the membrane (Fig. 2A(v and vi)). Using alignment marks that are part of the design, we ensure that the patterned electrodes on one side are coincident with the electrodes on the other side of the membrane. This makes the device amenable to tracking using time-lapse imaging, since the spacing between the interdigitated electrodes permits light to pass through and image cells as they migrate from one side to the other.

The microfluidic channel layers of the device were fabricated using a negative photoresist (SU-8) on a silicon (Si) wafer, creating a straight channel with a height of ≈100 μm. The patterned SU-8 Si wafer was used as a mold to hot emboss (Sublym, Eden Tech) and transfer the pattern to FlexdymTM (Eden Materials) thermoplastic sheets using a hot embosser (170 °C, 360 s). A glass slide was used as a substrate for assembling the layers that constitute the device (Fig. 2B(i)). The microfluidic channel that forms the bottom chamber was placed on the glass slide with the channel facing up. With the use of alignment marks on both the channel layer and the PET membrane, the PET membrane was aligned to the bottom microfluidic layer (Fig. 2B(ii)). Inlet and outlet holes of 2.5 mm diameter were punched in the top thermoplastic channel to access the channels (Fig. 2B(iii)). The top channel layer was then aligned with the channel side facing down, thereby making contact with the electrodes (Fig. 2B(iv)). The device was then placed in an oven at 80 °C for 1 min to thermal bond all layers conformally, and create water-tight interfaces to avoid leaks (Fig. 2B(v)). For reservoirs, polydimethyl siloxane (PDMS, Sylgard 184) slabs were cast on a silanized Si master and allowed to cross-link at 70 °C for 12 h. The slabs were then cut, and 5 mm through-holes were punched to serve as reservoirs. These reservoirs were O_2 plasma-bonded to the inlet and outlets of the device (Fig. 2B(vi)). Pictures of our experimental setup are shown in Fig. S2.

Cell culture

786-O cells were obtained from the American Type Culture Collection (ATCC) and cultured as described by the supplier. Cells were grown on polystyrene flasks in Roswell Park

§ Certain equipment, instruments, software, or materials are identified in this paper solely to provide a clear description of the experimental procedures. This identification does not constitute an endorsement or recommendation by NIST, nor does it imply that the materials or equipment mentioned are necessarily the most suitable or available for the stated purpose.

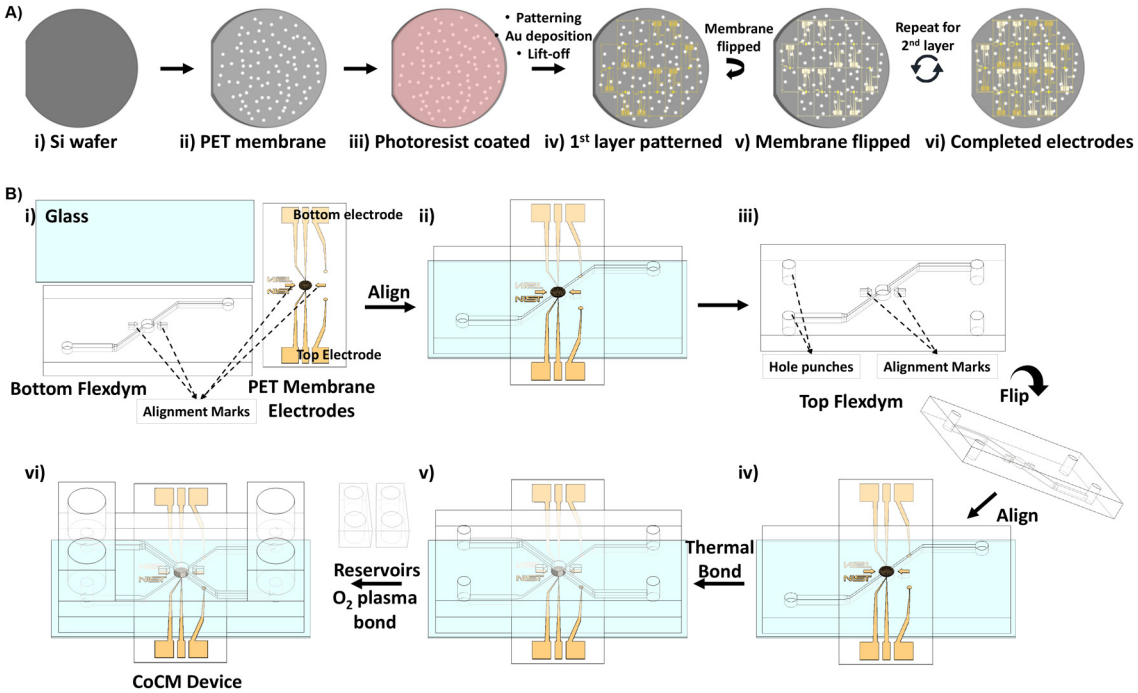

Fig. 2 Schematic of fabrication and assembly of CoCM device. A) Photolithography workflow for patterning electrodes on porous PET membrane. (i) A Si wafer with hPDMS, (ii) serves as a substrate for the PET membrane. (iii) Using standard photolithography processes, photoresist is coated on the membrane, (iv) patterned and deposited with gold, followed by lift-off to pattern one side of the electrodes. (v) The membrane is flipped, (vi) and the process is repeated to finish patterning electrodes on the other side of the membrane. B) Assembly and alignment of channel layers, PET membrane electrodes, and reservoirs for the CoCM device. (i–ii) A glass slide, the bottom channel layer, and the electrode are aligned using alignment marks. (iii) The top channel layer is hole punched, (iv) flipped and aligned with the electrode, followed by (v) thermal bonding. (vi) Reservoirs are plasma-bonded to the inlets and outlets to complete the CoCM device.

Memorial Institute (RPMI-1640) media supplemented with 10% fetal bovine serum (FBS) and sub-cultured upon reaching 80% percent confluency. All experiments were performed with cells below a passage number of 14. Before loading cells into the device, cells were stained with CellTracker Red in order to enable fluorescent live imaging of cell movement.

Cell seeding

To prepare for seeding cells, devices were sterilized by filling the channels and reservoirs with IPA for 30 min. Following IPA treatment, the channels were rinsed with DI water and then dried. The devices were then plasma cleaned using oxygen plasma to render surfaces hydrophilic. Channels were then coated with extracellular matrix (ECM) material to promote cell adhesion. First, the channels were treated with fibronectin (50 μg mL^{-1} in 1× PBS) for 2 h at room temperature, followed by polyallylamine hydrochloride (PAH) or poly-L-lysine (PLL) (0.5 mg mL^{-1} in deionized H_2O) for 30 min at room temperature.[35–37] Channels were then filled with media in preparation for cell seeding. Cells were seeded at a concentration of 2×10^6 mL^{-1} in the top channel. Briefly, 100 μL of cell suspension was added to the inlet of the top chamber, while ≈75 μL of media was added to the outlet of the top chamber. The offset in volumes at the inlet and outlet resulted in a slow, gentle flow of cells into the chamber. After 30 minutes, cells settle down and adhere to the top chamber. At this point, media/cell suspension in the inlets and outlets is replaced with fresh media.

Live-cell imaging

The device and a printed circuit board (PCB) were placed in a custom-made 3D printed holder. The holder allows for live-cell microscopy imaging while also providing for cable connections for electrical measurements and a 5% CO_2 line. The 3D printed chamber was then mounted on the microscope stage of an inverted microscope, which was encased in a heated chamber set to maintain 37 °C. Cells were imaged every 20 min for up to 72 h while the media was changed every 6 h. To obtain images of cells on the top surface of the membrane, the device was separately imaged with an upright microscope at the start and end of the experiment.

Monitoring cell migration across a porous membrane *via* impedance spectroscopy

The microfluidic chip consists of two vertically aligned chambers separated by a porous membrane. This region corresponds to the region of interest (ROI) where cells are seeded and observed, with independent inlet and outlet

microfluidic channels connecting the top and bottom chambers (see Fig. 3).

We tracked cell migration dynamics across the porous membrane using electrical impedance spectroscopy. Each side of the membrane contains a set of coplanar electrodes (Ti–Au) in a two-electrode measurement configuration, enabling impedance monitoring across the entire microfluidic chamber volume.[38] The measuring electrode is connected to ground and is designed with circular interdigitated features to facilitate spatial localization of cells through fluorescence microscopy (Fig. S1). A stimulating/excitation electrode is connected to an AC input signal of 30 kHz.[39–41] Each stimulating electrode is located at its corresponding microfluidic inlet branch, separated (4250 μm, center-to-center) from the microfluidic chamber measuring electrode, and has an effective area twice that of the measuring electrode. Each electrode pair is connected to a separate potentiostat channel (Parstat MC, PMC-1000, Ametek). Impedance data were acquired every 20 minutes using the VersaStudio software (version 2.65.2) loop function, with a 10-minute stagger between the triggering of each potentiostat channel to prevent inter-channel interference.

Cell staining

At the end of 72 h of cell migration tracking, calcein AM (1 μg mL^{-1} in non-supplemented RPMI-1640 media) was added to the channels and incubated at 37 °C for 45 min. The top and bottom surfaces of the membrane were then imaged using an inverted and upright microscope to obtain images of viable cells in each channel. Images were quantified using Fiji/ImageJ to determine the number of cells in each frame.

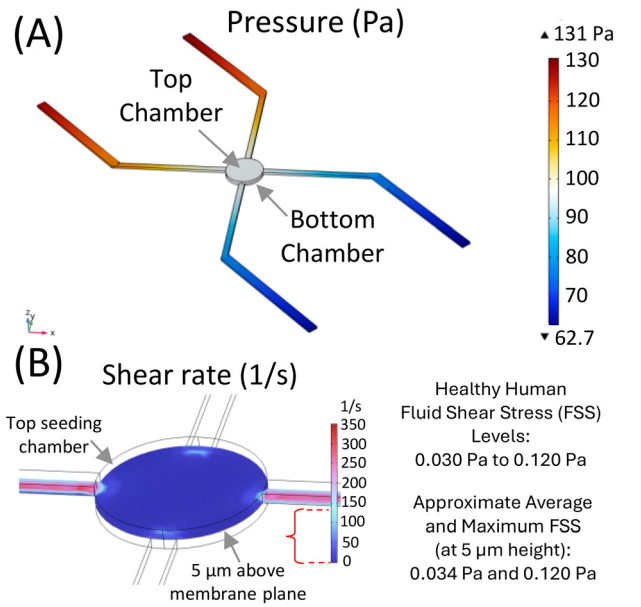

Fig. 3 CFD simulations of the CoCM microfluidic chip design. (A) Simulated pressure drop across the passive microfluidic device when inlet reservoirs are initially filled. (B) Shear rate distribution within the whole seeding chamber, showing an FSS slide at a height of 5 μm above the membrane, where the cells are adhered. The analysis ensures that cells are exposed to physiologically relevant FSS levels[42] that support cell viability for human kidney cells.

3 Results and discussion

Estimating fluid shear stress (FSS) *via* computational fluid dynamics (CFD) shear rate simulations to guide microfluidic cell seeding chamber design

Fluid shear stress (FSS) significantly influences cell viability, gene expression, and cellular functions.[42] Traditional cell culture platforms, such as well plates, are static systems characterized by a high volume-to-cell ratio. As a result, they present low FSS levels, which help preserve cell viability. In contrast, MPS devices often face challenges related to designing microchannels or culture chambers that maintain appropriate FSS levels. Active pumping in MPS offers greater flexibility because their flow rates can be easily adjusted to maintain FSS within physiologically relevant ranges, thereby preserving cell viability. Passive systems, such as the one described here, rely on gravity-driven flow, which makes FSS control more difficult. In these systems, careful geometric design is essential to ensure cells, particularly in regions of interest such as the seeding chamber, are not exposed to high FSS levels that could compromise their viability. Computational fluid dynamics (CFD) simulations are valuable tools for estimating flow conditions in gravity-driven microfluidic devices and for guiding design optimizations that minimize harmful FSS.

In our system, we seed cells in the top channel and concentrate the bulk cell population in our region of interest (ROI), where impedance electrodes monitor CoCM impedance. We simulated key parameters, such as the pressure drop (Fig. 3A), to optimize our device design. The system experiences the highest FSS immediately after each media change, when the inlet reservoirs are filled. Over time, FSS levels gradually decline until the system reaches quasi-equilibrium. This cycle repeats with each media replacement.

To assess the worst-case scenario, we used a finite element commercial software to simulate FSS under peak conditions immediately after changing the media. We estimated the shear rate experienced by the bulk cell population. For visualization purposes, we present an FSS slide plot at approximately 5 μm above the membrane surface (Fig. 3B). We show that the ROI FSS levels in the microfluidic chamber are within previously reported healthy FSS levels.[42] We calculated the FSS using the reported viscosity of RPMI-1640 medium at 37 °C,[43] which matches our experimental conditions. Based on these simulations, we ensured that most of the cells seeded on the membrane surface within our ROI would not be exposed to excessive FSS levels ($\gg$0.120 Pa) that could significantly affect their viability over the course of our experiment ($\approx$3 days).

CoCM impedance index

To account for baseline variability, impedance values were normalized separately for each channel using their respective initial measurements. Specifically, three impedance readings were acquired per hour and averaged to yield a single hourly value per channel. Each channel's hourly averages were then normalized by dividing them by that channel's average impedance during the first hour (t = 0 h), after seeding the cells on the top channel (≈30 min post-seeding). The normalized impedance for channel i at hour h was calculated using the following equation:

$$\tilde{Z}_{i,h}(\text{CoCM index}) = \frac{\sum_{n=1}^{N_h} Z_{i,h,n}}{\sum_{n=1}^{N_0} Z_{i,0,n}} \quad (1)$$

where $\tilde{Z}_{i,h,n}$ represents the nth impedance measurement for channel i (2 independent potentiostats) during hour h, N_h is the number of measurements taken in hour h, and N_0 is the number of measurements taken at t = 0 h (beginning of the experiment). This normalization reduces absolute impedance differences between channels that may arise from variations in chip connections, inconsistencies introduced during electrode fabrication, or slight offsets between potentiostats. This is necessary in order to account for differences in initial experimental conditions, such as one microfluidic chamber containing adherent cells while the other contains only media at t = 0 h. By expressing impedance relative to its respective channel baseline, this approach enables direct comparison of both channels over time and facilitates the assessment of whether impedance increases or decreases relative to each channel's initial state. We refer to this method of normalization, which enables real-time tracking of cells on both sides of the membrane, as the crossover cell migration impedance index, or CoCM index. Fig. S3 shows the stability of impedance measurements (CoCM index) over 6 hours in a device containing only culture medium (no cells), demonstrating minimal baseline variation.

Fluorescence imaging for validating CoCM and viability

We validated our impedance measurements with real-time fluorescence imaging. After manually seeding cells in the top chamber using passive flow, we imaged the cells with an upright microscope to confirm that we had enough cells in our ROI (Fig. 4A(i)). Our cell coverage density was approximately 500 mm^{-2}, forming multilayered clusters within the region of interest of the top chamber.

The chip was then placed in an inverted live-cell fluorescence microscopy setup, which included a closed environmental control system (37 °C, 5% CO_2, humidity

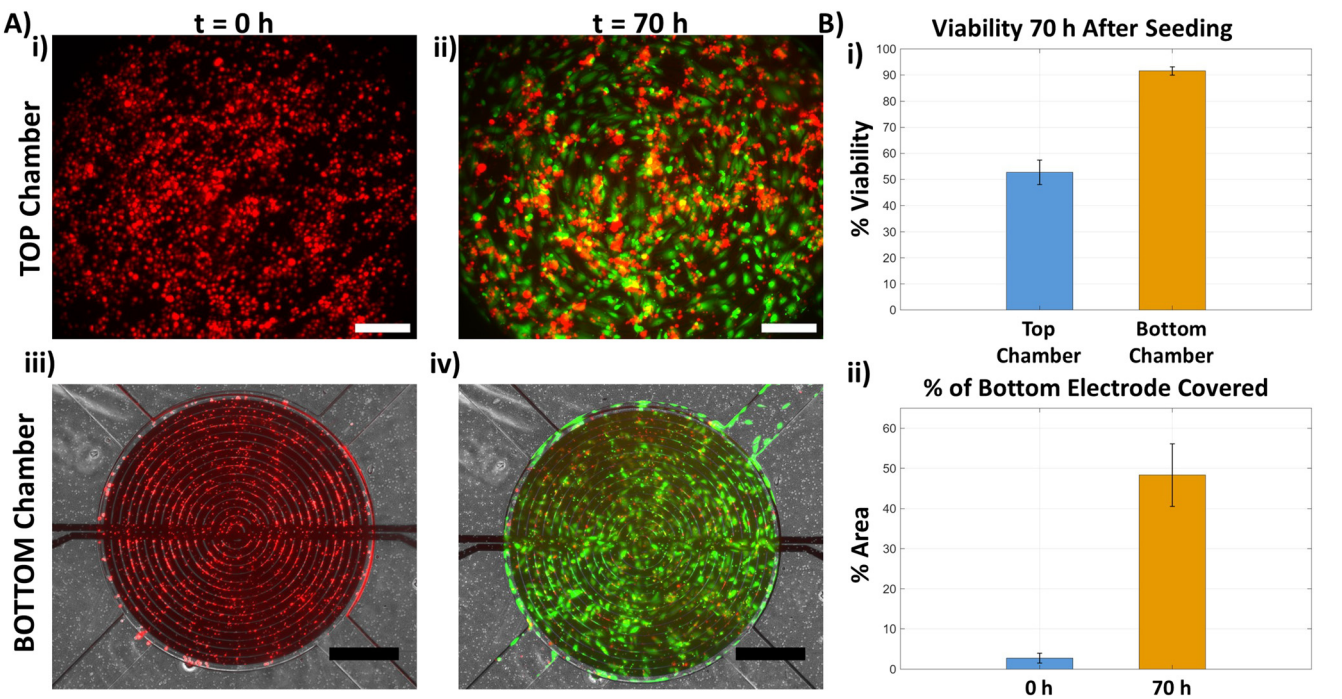

Fig. 4 Migration of 786-O cells from one side of the CoCM device to the other. A) (i) 786-O cells marked with CellTrackerRed are seeded in the top chamber at the start of the experiment (t = 0 h) (scale – 250 μm). (ii) At the end of the experiment (t = 70 h), cells are viable as demonstrated by the green calcein AM staining observed in live cells (scale – 250 μm). (iii) At the start of the experiment (t = 0 h), no cells are present in the bottom chamber (scale – 500 μm), (iv) while at the end (t = 70 h), cells that migrate are visible and viable as seen by the green calcein AM staining (scale – 250 μm). B) (i) Viability of cells in the top and the bottom chamber at the end of the experiment (t = 70 h) and (ii) the percentage of area covered by cells in the region of interest at the bottom electrode at the start (t = 0 h) and end of the experiment (t = 70 h). Data reported as mean ± STD.

maintained), for time-lapse impedance measurements in parallel with image acquisition. We acquired the first set of images at t = 0 h and took 3 images per hour over the course of 70 hours (approximately 3 days). At t = 0 h, only a few cells were in the focal plane of the inverted microscope, which was set to focus on the bottom side of the membrane, that is, on the opposite side of the seeding chamber (Fig. 4A(iii)). After 45 h, we observed cells crossing into the bottom chamber, as they began to overlay the interdigitated electrodes (see Movie S1). This behavior was consistent with our measured trends in the CoCM index, described later.

To verify that impedance measurements did not significantly affect cell viability, we performed a viability assay using calcein AM at the end of the experiment (t = 70 h) (Fig. 4A(ii) and (iv)). Live staining revealed dead cells in both chambers with >90% viable cells in the lower chamber, indicating that the applied voltage and frequency did not compromise cell viability and migration (Fig. 4B(i)). We attribute the lower viability in the top chamber to high cell density, which causes the stacking of cells in multiple layers, thereby resulting in a lack of cell spreading and formation of focal adhesions, leading to increased cell death. The area covered by the cells within the region of interest in the bottom chamber also increases as the cells migrate over the 70 h time period of the experiment (Fig. 4B(ii)). See Fig. S4 for a more detailed explanation of how we count the cells at the top and bottom channels while maintaining the same focal plane throughout the entire experiment.

CoCM index experimental results

We present CoCM index traces for n = 3, along with their corresponding standard deviations (±STD). Fig. 5(A) illustrates impedance changes across the top and bottom microfluidic chamber electrodes as cells migrate from the top (seeding) chamber to the bottom chamber through the porous membrane. As cells traverse the membrane, the CoCM index in the top chamber decreases. Conversely, the CoCM index in the bottom chamber begins to rise after approximately 10 hours, as shown in Fig. 5(B), indicating successful cell migration tracking.

In the top microfluidic chamber (blue line), the CoCM index decreases by approximately 20%, while in the bottom chamber (orange line), it increases by about 15%. A steeper change in the CoCM index occurs after 40 h, coinciding with a greater number of cells crossing the membrane. This trend is evident in the inversely proportional, symmetrical patterns shown in Fig. 5(C), and is corroborated by the corresponding fluorescent image frames shown in Fig. 5(D).

The image taken before the 40 hour mark (40 h after the beginning of the experiment at t = 0 h) shows most cells residing in the top chamber, on the opposite side of the

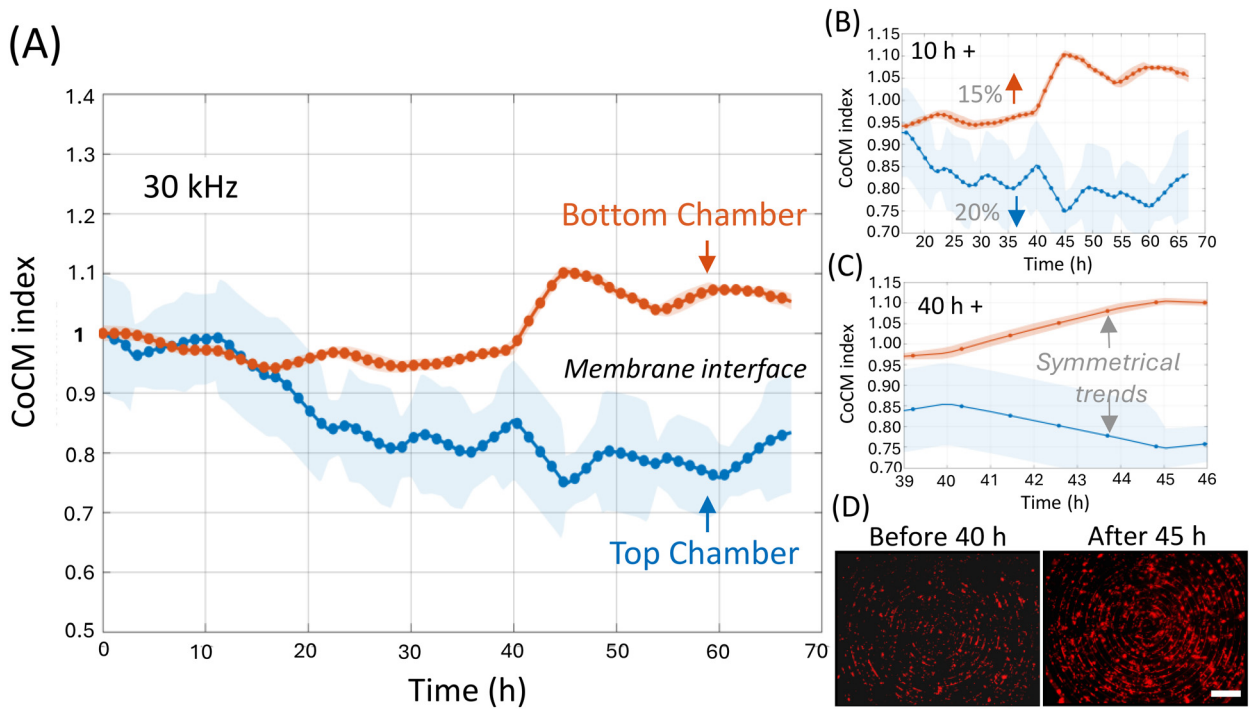

Fig. 5 CoCM index experimental results at 30 kHz frequency. (A) Top and bottom CoCM index plots for simultaneous impedance tracking at top and bottom chambers over the course of 70 h. (B) Close examination of the CoCM index plots in (A) starting at 10 h after seeding cells at the top chamber. At this time point, the 786-O cells impedance decreases ≈20% (blue line) at the top-side membrane electrodes and the impedance increases ≈15% (orange line) at the bottom-side membrane electrodes over the course of the experiment. (C) Symmetrical trends are observed 40 h after seeding the cells in the top chamber when a larger group of cells crosses to the bottom chamber. (D) Corresponding image cell tracking with fluorescent red cell-tracker dye (CMTPX) prior to 40 h and after 45 h, when the CoCM index presents a steeper and symmetrical CoCM index change correspondence between the top and bottom measurements (scale – 250 μm).

membrane. Due to the inverted microscope's focal plane being aligned with the bottom-facing membrane electrodes, the electrodes obstruct the light and obscure the cells in the top chamber. In contrast, the image taken shortly after 45 hours shows cells clearly in focus at the bottom electrode. At this point, the cells have crossed the membrane/electrode surface and are now positioned at the focal plane of the inverted microscope, where it can focus and capture clear images of the cells.

Enhanced cell detection *via* small detection volume

Our microfluidic chip's chamber electrodes have a small surface area-to-detection volume ratio (SA/V) of $\approx 0.005\ \mu m^{-1}$, enhancing the interaction between our impedance sensors and the cells. This design enabled us to monitor cell migration with high resolution, as demonstrated in Fig. 5, where we observed impedance changes in response to small numbers of migrating cells. This is especially true for the bottom chamber, where cells crossed, spread, and began to form a monolayer, resulting in a tighter standard deviation range compared to the top chamber, where cells formed multilayered, heterogeneous stacks. Accordingly, the data show a larger standard deviation at each measurement time point in the top chamber. To establish the baseline variability of our system, initial background measurements in a cell-free device yielded a coefficient of variation (CV) of 3.21%, with a 95% confidence interval ranging from 1.73% to 4.70%, indicating low experimental variation (<5%).

Advantages and limitations of our current passive flow setup

Our microfluidic device operates with gravity-driven flow, a design choice that simplifies fluid handling by eliminating the need for external pumps. This passive flow setup is easy to use and offers advantages in terms of reduced complexity and cost, as it requires no active fluid pumps or complex tubing connections. The system's simplicity is enhanced by the integration of reservoirs in the inlets and outlets, which serve as built-in fluid buffers. These reservoirs do not require a significant footprint or height, making the setup ideal for situations with limited microscope head clearance and minimizing the need for additional external components.

However, while passive flow improves ease of use and simplifies fluid handling, it also presents several challenges. One of the primary drawbacks is that maintaining a constant volumetric flow becomes more difficult, even when there is continuous positive pressure flow. Achieving stable flow rates over time is a challenging task. Particularly in our case, after the system reaches equilibrium and the flow becomes quasi-static, similar to a conventional well plate setup, but with a significantly reduced volume-to-cell ratio. Therefore, the impact of medium evaporation on the composition becomes more pronounced compared to a well plate. Additionally, the small volume of the microfluidic chamber means that when the nutrients in the medium are depleted by the cells, more nutrients need to travel by diffusion from longer distances through the length of the channel, further compounding the issue.

To mitigate the effects of evaporation and medium depletion, we fabricated our microfluidic devices using a biocompatible and less gas-permeable co-polymer material (Flexdym). This helped slow down medium evaporation. However, despite these efforts, medium depletion still occurred after the fluid flow equilibrated at both inlets and outlets. As a result, we need to replenish the media every 6 to 8 hours to maintain optimal cell viability.

Our platform offers a significant advantage over commercially available systems for cell migration studies by integrating interdigitated electrodes on both sides of a porous membrane embedded within a microfluidic system. Unlike well-known static, transwell-based commercial platforms, which monitor impedance only on one side of the membrane[23,24] and cannot capture cell movement across the pores (cross-over cell migration, CoCM), our device enables real-time impedance tracking of cells on both sides, allowing comprehensive monitoring of the migration process. Our microfluidic device supports passive, pump-free flow conditions similar to traditional transwells, while also opening the possibility for dynamic, pump-driven flow to better mimic physiological shear stresses and mass transport. In addition, our system also couples real-time optical imaging, providing a multi-modal approach to studying cell migration. Finally, we fabricated our devices using the aforementioned biocompatible thermoplastic block copolymer, which is compatible with other commercially available thermoplastics and microfabrication techniques, allowing for further integration into scalable microfluidic arrays.

4 Conclusions

We developed a fabrication method to pattern gold electrodes on both sides of a porous PET membrane. These two independently addressable arrays of electrodes enable simultaneous impedance measurements on both sides of the membrane, thus allowing for complete monitoring of cell migration through the membrane or CoCM. In addition, we introduced the CoCM impedance index, a method to normalize impedance measurements on both membrane surfaces, which provides real-time tracking of cells as they migrate from the top chamber, where they are initially seeded, to the bottom chamber, which initially contains only media. The small surface area-to-volume (SA/V) ratio of our microfluidic device on both sides of the porous membrane interface allows us to resolve impedance changes as small groups of cells migrate through the membrane pores. The microfluidic design was carefully optimized to maintain fluid shear stress (FSS) within physiologically relevant ranges. This is critical for maintaining viable cells throughout the length of the experiments. Furthermore, we fabricated the microfluidic channels using a biocompatible, thermally bonded copolymer capable of withstanding pressurized conditions.

This makes our device suitable for pump-driven flows while remaining adaptable to a wide range of microphysiological systems (MPS).

Author contributions

Conceptualization: Karina Torres-Castro, Aditya Rane, Darwin R. Reyes; resources, supervision, and project administration: Darwin R. Reyes; investigation, methodology, formal analysis & data curation: Karina Torres-Castro, Aditya Rane; software: Karina Torres-Castro; writing – original draft-review: Karina Torres-Castro, Aditya Rane; writing – review & editing: Karina Torres-Castro, Aditya Rane, Darwin R. Reyes.

Conflicts of interest

The authors declare no conflicts of interest.

Data availability

The data supporting this article have been included as part of the supplementary information (SI).

Supplementary information: Fig. S1–S4 and Movie 1 with further experimental details. See DOI: https://doi.org/10.1039/d5lc00898k.

Acknowledgements

This work was performed under financial assistance award 70NANB23H031 and 70NANB22H160 from the National Institute of Standards and Technology, U.S. Department of Commerce. The statements, findings, conclusions, and recommendations are those of the author(s) and do not necessarily reflect the views of the National Institute of Standards and Technology or the U.S. Department of Commerce (K. T.-C. was supported under 70NANB23H031, and A. R. was supported under 70NANB22H160). D. R. R. was supported by the National Institute of Standards and Technology (NIST) internal funds. Portions of this work were conducted at the NIST Center for Nanoscale Science and Technology (CNST).

References

1 A. Luster, R. Alon and U. von Andrian, *Nat. Immunol.*, 2005, **6**, 1182–1190.
2 D. Molino, S. Quignard, C. Gruget, F. Pincet, Y. Chen, M. Piel and J. Fattaccioli, *Sci. Rep.*, 2016, **6**, 1–11.
3 P. Friedl and K. Wolf, *Nat. Rev. Cancer*, 2003, **3**, 362–374.
4 S. SenGupta, C. Parent and J. Bear, *Nat. Rev. Mol. Cell Biol.*, 2021, **22**, 529–547.
5 C. Marchant, A. Malmi-Kakkada, J. Espina and E. Barriga, *Nat. Mater.*, 2022, **21**, 1314–1323.
6 B. Majhy, P. Priyadarshini and A. K. Sen, *RSC Adv.*, 2021, **11**, 15467–15476.
7 I. Guido, D. Diehl, N. Olszok and E. Bodenschatz, *PLoS One*, 2020, **15**, e0239379.
8 Z. Roveimiab, F. Lin and J. E. Anderson, *Am. J. Physiol.*, 2020, **319**, C75–C92.
9 K. Singh, K. M. Hotchkiss, K. K. Patel, D. S. Wilkinson, A. A. Mohan, S. L. Cook and J. H. Sampson, *Cancers*, 2021, **13**, 5367.
10 R. Alert and X. Trepat, *Annu. Rev. Condens. Matter Phys.*, 2020, **11**, 77–101.
11 S. Seetharaman and S. Etienne-Manneville, *Trends Cell Biol.*, 2020, **30**, 720–735.
12 D. Ingber, *Nat. Rev. Genet.*, 2022, **23**, 467–491.
13 I. C. Fortunato and R. Sunyer, *Biophysica*, 2022, **2**, 548–563.
14 A. Shellard and R. Mayor, *Trends Cell Biol.*, 2020, **30**, 852–868.
15 T. Gerasimenko, S. Nikulin, G. Zakharova, A. Poloznikov, V. Petrov and A. Baranova, *Front. Bioeng. Biotechnol.*, 2020, **7**, 474.
16 S. E. De León, A. Pupovac and S. L. McArthur, *Biotechnol. Bioeng.*, 2020, **117**, 1230–1240.
17 Q. Hassan, S. Ahmadi and K. Kerman, *Micromachines*, 2020, **11**, 590.
18 Z. Zhang, X. Huang, K. Liu, T. Lan, Z. Wang and Z. Zhu, *Biosensors*, 2021, **11**, 470.
19 L. Yang, L. Arias, T. Lane, M. Yancey and J. Mamouni, *Anal. Bioanal. Chem.*, 2011, **399**, 1823–1833.
20 G. Mijares, D. Reyes, J. Geist, M. Gaitan, B. Polk and D. DeVoe, *J. Res. Natl. Inst. Stand. Technol.*, 2010, **2**, 61–73.
21 J. Fernandes, N. Karra, J. Bowring, R. Reale, J. James, C. Blume, T. J. Pell, W. C. Rowan, D. E. Davies, E. J. Swindle and H. Morgan, *Lab Chip*, 2022, **22**, 2041–2054.
22 Y.-S. Chen, C.-H. Huang, P.-C. Pai, J. Seo and K. F. Lei, *Biosensors*, 2023, **13**, 2079–6374.
23 *A. C. analysis xCELLigence*, Agilent Technologies Inc., 2019.
24 *Real-Time and Dynamic Monitoring of Cell Proliferation and Viability for Adherent Cells*, Agilent Technologies Inc, 2020.
25 C. Bird and K. Shelli, *Nat. Methods*, 2009, **6**, v–vi.
26 E. Primiceri, M. S. Chiriacó, F. Dioguardi, A. G. Monteduro, E. D'Amone, R. Rinaldi, G. Giannelli and G. Maruccio, *Lab Chip*, 2011, **11**, 4081–4086.
27 P. Bouchalova and P. Bouchal, *Cancer Cell Int.*, 2022, **22**, 394.
28 Y. Shi, S. Sun, H. Liu, M. Zhao, M. Qin, J. Liu, J. Hu, Y. Zhao, M. Li, L. Zhang and C. Huang, *Lab Chip*, 2025, **25**, 253–262.
29 H. Nazari, J. Shrestha, V. Y. Naei, S. R. Bazaz, M. Sabbagh, J. P. Thiery and M. E. Warkiani, *Biosens. Bioelectron.*, 2023, **234**, 115355.
30 O. Y. F. Henry, R. Villenave, M. J. Cronce, W. D. Leineweber, M. A. Benz and D. E. Ingber, *Lab Chip*, 2017, **17**, 2264–2271.
31 Z. Izadifar, B. Charrez, M. Almeida, S. Robben, K. Pilobello, J. van der Graaf-Mas, S. L. Marquez, T. C. Ferrante, K. Shcherbina, R. Gould, N. T. LoGrande, A. M. Sesay and D. E. Ingber, *Biosens. Bioelectron.*, 2024, **265**, 116683.
32 T. A. Nguyen, T.-I. Yin, D. Reyes and G. A. Urban, *Anal. Chem.*, 2013, **85**, 11068–11076.
33 C. Hanke, P. S. Dittrich and D. R. Reyes, *ACS Appl. Mater. Interfaces*, 2012, **4**, 1878–1882.
34 A. Gangopadhyay, B. J. Nablo, M. V. Rao and D. R. Reyes, *Adv. Eng. Mater.*, 2017, **19**, 1600592.
35 D. R. Reyes, J. S. Hong, J. T. Elliott and M. Gaitan, *Langmuir*, 2011, **27**, 10027–10034.

36 K. Bhadriraju, J. S. Hong, S. P. Lund and D. R. Reyes, *ACS Biomater. Sci. Eng.*, 2017, **3**, 2559–2569.
37 S. P. Forry, D. R. Reyes, M. Gaitan and L. E. Locascio, *J. Am. Chem. Soc.*, 2006, **128**, 13678–13679.
38 C. Honrado, P. Bisegna, N. S. Swami and F. Caselli, *Lab Chip*, 2021, **21**, 22–54.
39 S. Abasi, J. R. Aggas, G. G. Garayar-Leyva, B. K. Walther and A. Guiseppi-Elie, *ACS Meas. Sci. Au*, 2022, **2**, 495–516.
40 F. Witzel, R. Fritsche-Guenther, N. Lehmann, A. Sieber and N. Blüthgen, *Bioinformatics*, 2015, **31**, 2705–2712.
41 C. R. Keese, K. Bhawe, J. Wegener and I. Giaever, *BioTechniques*, 2002, **33**(4), 842–850.
42 E. Ross, E. Gordon, H. Sothers, D. Roshan, B. Oakley, D. Haithcock, P. Belabhaskar, K. Pant, M. Myers, S. Cooper and N. Cox, *Sci. Rep.*, 2021, **11**, 14053.
43 C. Poon, *J. Mech. Behav. Biomed. Mater.*, 2022, **126**, 105024.